

# Supporting Information: Angle-resolved cathodoluminescence imaging polarimetry

Clara I. Osorio,<sup>†,‡</sup> Toon Coenen,<sup>†,‡</sup> Benjamin Brenny,<sup>†,‡</sup> Albert Polman,<sup>†</sup> and A.

Femius Koenderink<sup>\*,†</sup>

*Center for Nanophotonics, FOM Institute AMOLF, Science Park 104, 1098 XG Amsterdam, The  
Netherlands*

E-mail: f.koenderink@amolf.nl

## Spectral measurements on bullseye

To study the spectral response of the bullseye from Fig. 2 (main text), we raster scan the electron beam over the central part of the structure in 15 nm steps, and collect a CL spectrum for every pixel using a visible/NIR fiber-coupled Czerny-Turner spectrometer.<sup>1</sup> The scan includes the central plateau, the first groove, and part of the first ridge. The spectra are corrected for the system response using the TR emission of the unstructured gold substrate.<sup>2</sup> We then radially average the spectrum to obtain a map showing emitted intensity as a function of wavelength and radius, taking into account the proper Jacobian so we can directly compare the intensities (shown in Fig. S1(a)). Figure S1(b) shows individual spectra for specific radial distances as indicated in (a) by the white dashed lines.

We observe several features in the scan. On the plateau, the emission is quite broadband except for a strong dip in intensity around  $\lambda_0 = 650$  nm. The CL intensity increases towards the edge of

---

<sup>\*</sup>To whom correspondence should be addressed

<sup>†</sup>Center for Nanophotonics, FOM Institute AMOLF, Science Park 104, 1098 XG Amsterdam, The Netherlands

<sup>‡</sup>These authors contributed equally to this work

the plateau, then drops in the groove, and becomes bright on the first ridge again. The observed spectral features can be attributed to a mix of resonant and diffractive effects.

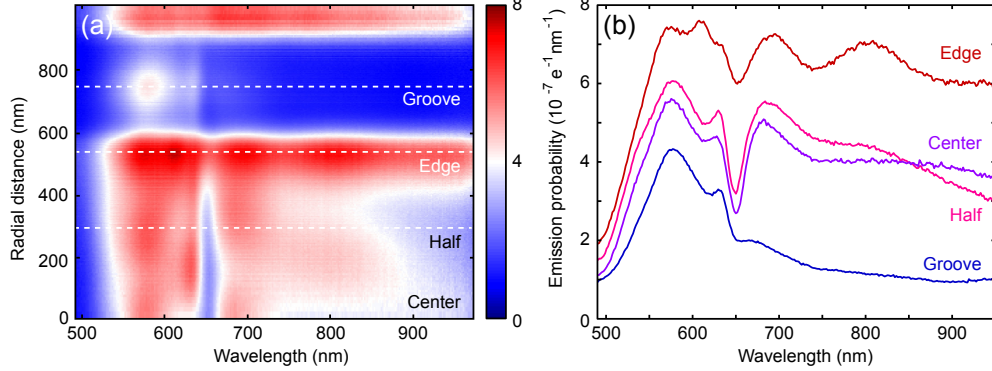


Figure S1: (a) CL intensity as a function of wavelength and radial position from the center of the bullseye. The spectra are corrected for dark noise and the spectral response of the detection system. (b) CL spectra at selected radial positions corresponding to the center, halfway, and the edge of the bullseye plateau. We also show a spectrum for excitation in the center of the first groove. The positions are indicated by the white dashed lines in (a). Notice that the color bar in (a) and the vertical axis in (b) both correspond to emission probability.

Because the groove is wide enough, it supports a zero-th order standing wave mode on the bottom of the groove around  $\lambda_0 = 580$  nm, which is cut-off for longer wavelengths leading to a low intensity in the red.<sup>3,4</sup> The dip at  $\lambda_0 = 650$  nm can be attributed to an interesting experimental artifact related to the diffraction of SPPs. Consistent with the grating equation mentioned in the main text, the bullseye emits very close to the normal at this wavelength. Because the bullseye structure is highly directional, a major part of this diffracted beam is lost through the  $600 \mu\text{m}$  hole in the mirror right above the sample. In fact, one could use this dip to find the wavelength and spatial position at which such a structure attains maximum directionality in the normal direction. In this case, the effect is strongest for the central positions in the bullseye because the beam is exactly normal to the sample as is visible in Fig. 3(a) for  $\lambda_0 = 750$  nm. Even though the dip is strongest in the center of the plateau, it is visible for every radial excitation position in this map (even within the groove), indicating that the extended bullseye geometry always causes a significant fraction of CL emission to be in the normal direction.

## Calculation of the Mueller matrices

The Mueller matrix of an optical element accounts for the effect of the element on the polarization state of an incident field.<sup>5</sup> The Mueller matrices of a linear polarizer and a QWP are well-known for example. We use the Mueller formalism to relate the Stokes vector in the detection plane to the Stokes vector describing the sample emission polarization. The resulting Mueller matrix of the mirror contains both geometric and polarizing effects of the mirror in the emission polarization.

To retrieve the Mueller matrix of our light collection system, we calculate how the electric field components  $E_\theta$  and  $E_\phi$  in the emission plane transform to  $E_y$  and  $E_z$  in the detection plane.<sup>6,7</sup> To that end we calculate how fully isotropic  $p$ -polarized and  $s$ -polarized emission is projected onto the detection plane by the parabolic mirror. We use the geometrical methods described in section 3 of Ref.<sup>8</sup> to account for the parabolic reflector and we use the full complex Fresnel reflection coefficients to accurately describe the light reflection on the mirror. These coefficients were calculated using tabulated optical constants<sup>9</sup> for the central frequency of the collection bandwidth. As the reflection angle at the mirror is different for every wave-vector emanating from the sample, each element of the Mueller matrix is a function of the emission angle.<sup>6,7</sup> Instead of calculating the Mueller matrix, one could also envision experimentally retrieving it. This requires a precisely controlled radial and azimuthal polarization source as standard. While transition radiation could serve as a fully radial source, a fully azimuthal source is not readily available.

The Mueller matrices can be used in two directions. Either one can invert measured data from the detector plane to sample coordinates, or in the opposite direction, one can predict how a given source will appear on the detector plane. For our analysis of TR emission, in Fig. S2 we apply Mueller matrices to theoretical TR emission to predict the measured data for each setting of the polarimeter. In this case, we combine the mirror Mueller matrix with the Mueller matrices of a linear polarizer and a QWP, which are a function of the selected analyzer angles  $\alpha$  and  $\beta$ .<sup>10</sup> We note that for fully polarized sources this is analogous to the approach in Ref.<sup>8</sup> where the Jones matrix of the polarizing element operates on the Jones electric field vector.

## Polarimetry of transition radiation emission

Transition radiation (TR) emission occurs whenever an electron traverses an interface between two dielectric media. The electron locally polarizes the material close to the interface, giving rise to a well-defined broadband vertically-oriented point-dipole-like source.<sup>8,11,12</sup> This makes it a useful source to test our CL polarimetry technique. Here we perform polarimetry measurements on an unstructured part of the single-crystal Au substrate from which only TR emission is expected, using the same technique used for the bullseye. Figure S2(a) shows the TR data at  $\lambda_0 = 850$  nm for every polarimeter setting. The top left panel includes the angular coordinate system for reference.

In addition to the TR measurements, we calculated the emission pattern for a z-oriented dipole on top of an Au substrate and its polarization components. The dipolar far-field for  $\lambda_0 = 850$  nm was calculated from the asymptotic far-field expressions<sup>13</sup> using ellipsometry data for the optical constants of the gold substrate. We then calculate the expected filtered pattern using the appropriate Mueller matrices for the paraboloid mirror and the polarimeter components. Figure S2(b) shows the result of this calculation including the angular acceptance of the mirror, in order to allow a good comparison with the data. The excellent agreement of both angular distributions and relative intensities between data and calculation indicates that TR emission is indeed dipolar and that the mirror correction works well. The fringes in the data are an experimental artifact, probably due to interference between multiple reflections of the optical elements on the detector.

We can use the measurements from Fig. S2(a) to determine the Stokes parameters in the detection plane of the CCD and then use the Mueller matrix formalism to correct for the effects of the mirror. This allows us to retrieve the Stokes parameters in the sample plane from which we can determine the different field amplitudes. Figure S2(c) shows the Stokes parameters in both the detection and sample planes, where  $S_1$ ,  $S_2$  and  $S_3$  have been normalized by  $S_0$  so that we can clearly observe the polarization distortions due to the mirror. In the detection plane the Stokes parameters display complex patterns that are very similar to those shown for the bullseye in Fig. 2(c), since both cases are dominated by purely radial polarization. In the sample plane the behavior of the Stokes parameters is much simpler,  $S_0$  has barely changed and  $S_1$  is close to 1 while  $S_2$  and  $S_3$  are

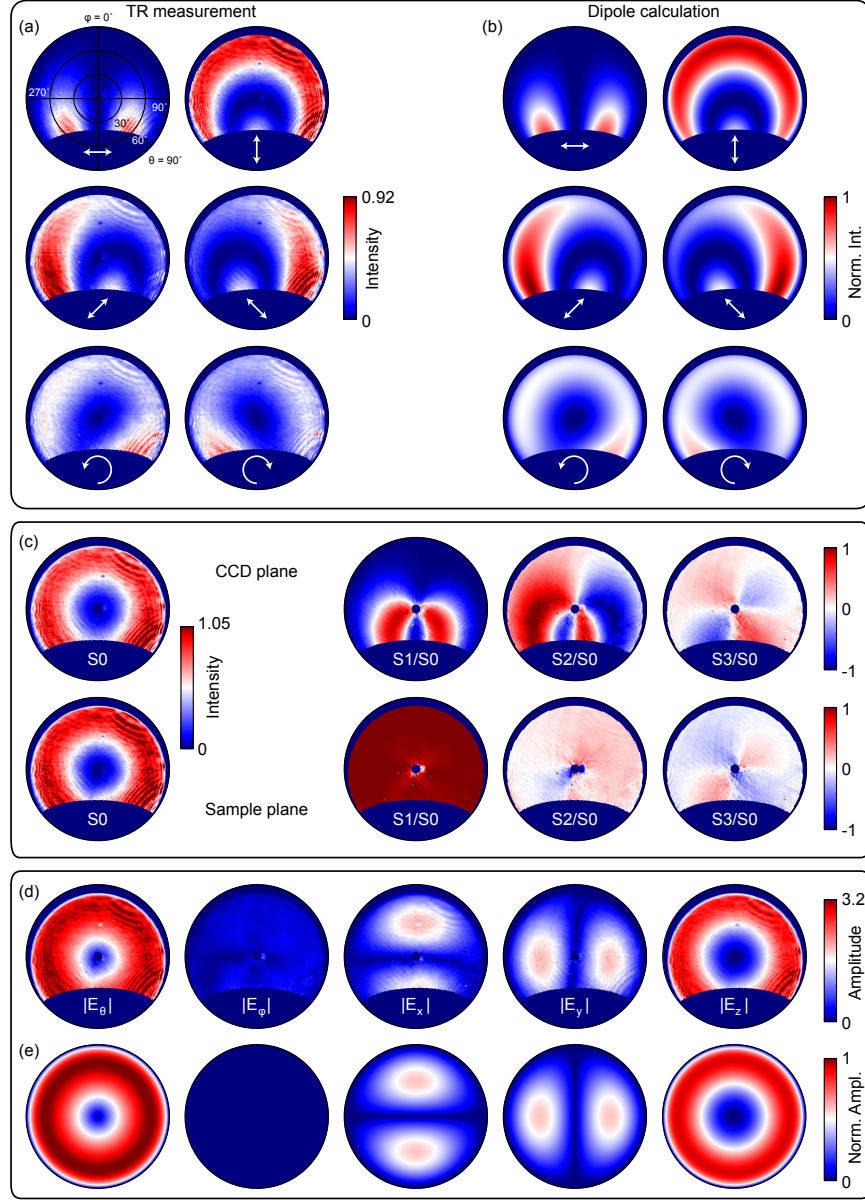


Figure S2: (a) Polarization-filtered angular CL patterns of TR emission for a Au single crystal for different analyzer settings as indicated by the white arrows, measured at  $\lambda_0 = 850$  nm. (b) Calculated polarization-filtered patterns for a vertically oriented point-dipole source on top of a gold substrate (at  $\lambda_0 = 850$  nm). (c) Stokes parameters as a function of angle in the CCD plane as well as in the sample plane, after the mirror correction. The  $S_1$ ,  $S_2$ , and  $S_3$  patterns are normalized to  $S_0$  to better show the overall polarization distribution. (d) Spherical and cartesian field amplitude distributions as a function of angle, retrieved from the experimental data in (a). (e) Calculated field amplitudes for a vertical dipole.

very small. Again, TR is expected to be fully radially polarized, so there should be no diagonal ( $S_2$ ) or circular ( $S_3$ ) components. The striking difference between the Stokes parameters in the two

planes underscores the importance of the Mueller matrix correction to provide accurate results.

Fig S2(d) shows the spherical and Cartesian field amplitudes that have been retrieved from the Stokes parameters in sample space. The fields nicely reveal the expected radially polarized nature of the emission. The amplitudes have been plotted using a single color scale to allow a quantitative comparison between the different components. Both the relative amplitudes and amplitude distributions match very well with the calculated dipolar fields shown in (e). These results demonstrate that cathodoluminescence polarimetry can reliably be used as a quantitative tool for deducing the far-field polarization distribution of a nanoscale emitter.

## Silicon and GaAs polarimetry

Calculating the contributions of TR, polarized and unpolarized luminescence to the total emission from Si or GaAs requires determining their angular profiles. An essential part of this process are the transmission coefficients  $T_p$  and  $T_s$  at the sample-vacuum interface, shown in Fig. 5(a) for the case of Si at  $\lambda_0 = 650$  nm. The large contrast between the two coefficients at angles above  $\sim 20^\circ$  leads to more  $p$ -polarized light exiting the Si than  $s$ -polarized light. Especially near the Brewster angle, the  $p$ -component of the field is transmitted significantly better than the  $s$ -component, with a contrast between intensity transmission  $T_p$  and  $T_s$  exceeding 4 (see Fig. 5(a)). This difference in transmission coefficients results in a CL emission profile slightly different than the Lambertian  $\cos(\theta)$  profile (blue curve in Fig. S3(b)). The polarizing effect of the interface does not noticeably affect the emission pattern of the total luminescence, but the unpolarized luminescence (consisting of equal amounts of  $s$ - and  $p$ -polarized light) is markedly narrower. Accordingly, the polarized part of the luminescence is stronger at higher angles and, interestingly, it follows a very similar profile to that of TR for Si at  $\lambda_0 = 650$  nm, which has been calculated using formulas derived in Ref.<sup>11</sup> The same formulas are used to calculate the gray line describing TR from Au at  $\lambda_0 = 850$  nm in Fig. 5(a).

Once the theoretical profiles for the different emission processes are calculated, it is possible to determine their relative contributions to the total emission. The fraction of polarized and unpo-

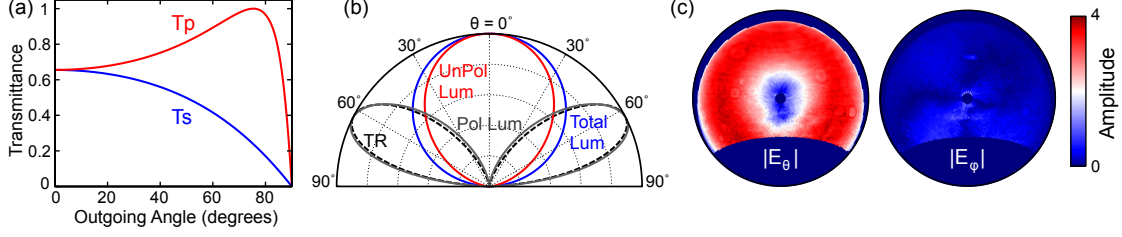


Figure S3: (a) Transmission coefficients  $T_p$  and  $T_s$  at the sample-vacuum interface at  $\lambda_0 = 650$  nm for Si, as a function of the internal angle of emission. (b) Calculated normalized angular emissions patterns of the different contributions to Si CL emission. The total luminescence profile (blue) as well as the unpolarized (red) and polarized (grey) luminescence contributions are shown together with the theoretical TR profile (black dashed line). (c)  $|E_\theta|$  and  $|E_\phi|$  field amplitudes of the polarized emission from Si, in units of  $10^2 \sqrt{ADU sr^{-1} s^{-1}}$ .

larized luminescence is fully specified by the Fresnel equations. This gives enough information to compare calculations to data from GaAs with very good agreement, as that is fully dominated by luminescence. The case of Si is more complex as TR also plays a role, so the polarized emission is comprised of coherent TR as well as polarized luminescence. We determine the ratio of TR and luminescence by fitting the total intensity ( $S_0$ ) to a linear combination of the two processes. Fresnel calculations again predict the polarized and unpolarized contributions to the luminescence so that we can combine all three components. For both the calculations and the experiments we scale the angular distributions by the overall (integrated) emission intensity, and find good (absolute) agreement, as was shown in Fig. 5(b). The polarized signal constitutes  $\sim 32\%$  of the total emission. More explicitly, we find that TR contributes  $\sim 21\%$  of the total CL intensity, so polarized luminescence contributes  $\sim 11\%$  and unpolarized luminescence  $\sim 68\%$ .

After separating the polarized and unpolarized components we can retrieve the different electric field components. Both the TR and the polarized luminescence should be  $p$ -polarized, which we verify from the experimental data using the Mueller analysis to determine the radial and azimuthal field amplitudes. This is shown for Si in Fig. S3(c), where we indeed observe that almost all of the amplitude is in the  $|E_\theta|$  component, i.e. for  $p$ -polarization. This demonstrates that we can separate the unpolarized and polarized emission even from mostly incoherently radiating semiconductors and still retrieve the correct electric fields for the polarized portion of the emission.

## References

- (1) Coenen, T.; Vesseur, E. J. R.; Polman, A.; Koenderink, A. F. Directional emission from plasmonic Yagi Uda antennas probed by angle-resolved cathodoluminescence spectroscopy. *Nano Lett.* **2011**, *11*, 3779–3784.
- (2) Kuttge, M.; Vesseur, E. J. R.; Koenderink, A. F.; Lezec, H. J.; Atwater, H. A.; García de Abajo, F. J.; Polman, A. Local density of states, spectrum, and far-field interference of surface plasmon polaritons probed by cathodoluminescence. *Phys. Rev. B* **2009**, *79*, 113405.
- (3) Brucoli, G.; Martín-Moreno, L. Effect of defect depth on surface plasmon scattering by sub-wavelength surface defects. *Phys. Rev. B* **2011**, *83*, 075433.
- (4) Schoen, D. T.; Coenen, T.; García de Abajo, F. J.; Brongersma, M. L.; Polman, A. The planar parabolic optical antenna. *Nano Lett.* **2013**, *13*, 188–193.
- (5) Born, M.; Wolf, E. *Principles of Optics: Electromagnetic Theory of Propagation, Interference and Diffraction of Light*, 7<sup>th</sup> edition; Cambridge University Press, 1997.
- (6) Rodríguez-Herrera, O. G.; Bruce, N. C. Confined three-dimensional plasmon modes inside a ring-shaped nanocavity on a silver film imaged by cathodoluminescence microscopy. *Opt. Eng.* **2006**, *45*, 053602.
- (7) Rodríguez-Herrera, O. G.; Rosete-Aguilar,; Bruce, N. C. Cambio del estado de polarización en un espejo elíptico. *Rev. Mex. Fis.* **2004**, *E50*, 33–40.
- (8) Coenen, T.; Polman, A. Polarization-sensitive cathodoluminescence Fourier microscopy. *Opt. Express* **2012**, *20*, 18679–19691.
- (9) Palik, E. D. *Handbook of optical constants*; Academic Press, New York, 1985.
- (10) Chipman, R. A. In *Handbook of Optics, Third Edition Volume I: Geometrical and Physical Optics, Polarized Light, Components and Instruments*, 3rd ed.; Bass, M., DeCusatis, C.,



Enoch, J., Lakshminarayanan, V., Li, G., Macdonald, C., Mahajan, V., Van Stryland, E., Eds.; McGraw-Hill, Inc.: New York, NY, USA, 2010.

- (11) García de Abajo, F. J. Optical excitations in electron microscopy. *Rev. Mod. Phys.* **2010**, *82*, 209–275.
- (12) Coenen, T.; Vesseur, E. J. R.; Polman, A. Angle-resolved cathodoluminescence spectroscopy. *Appl. Phys. Lett.* **2011**, *99*, 143103.
- (13) Novotny, L.; Hecht, B. *Principles of nano-optics*; Cambridge University press, 2006.